Supporting Information

Electroreduction of Carbon Dioxide to Formate using Highly Efficient Bimetallic Sn-Pd Aerogels

Maryam Abdinejad,*[‡a] Mozhgan Khorasani Motlagh,[‡b] Meissam Noroozifar,[b] and Heinz Bernhard Kraatz*[b,c]

a. Department of Chemical Engineering, Delft University of Technology, Van der Maasweg 9 2629 HZ Delft, the Netherlands

b. Department of Physical and Environmental Sciences, University of Toronto Scarborough, 1265 Military Trail, Toronto, ON M1C 1A4, Canada

c. Department of Chemistry, University of Toronto, 80 St. George Street, Toronto, ON M5S 3H6, Canada

Table of Contents:

Part S1. Reagents and Chemicals **2**

Part S2. Material Characterizations **2**

Part S3. Synthesis of the Sn-Pd Aerogels **3**

Part S4. Electrochemical Measurements **4**

Part S5. Electrochemical active surface area measurement **8**

Part S5. References **16**

Part S1. Reagents and Chemicals

All reagents and solvents were of commercial reagent grade and were used without further purification, except where noted. $SnCl_4$ (99%), H_2SO_4 (≥99.99%), K_2CO_3 (99.99%), H_2PdCl_4 (99%), glyoxylic acid monohydrate (97%), Chloroform d (>99.8%D), Nafion perfluorinated ion-exchange resin (5%), CNT (outer diameter 13–18 nm, length 3–30 μm, purity> 99% and functional content 7.0% ± 1.5%) were purchased from Sigma-Aldrich Company. All the experimental solutions were prepared using deionized water purified by a Millipore Milli-Q water purification system (18.2 MΩ cm).

Part S2. Material Characterizations

All of the spectroscopy data for the structural characterizations were obtained using the research facilities at the University of Toronto and Delft University of Technology The concentration of gaseous products (H_2) was obtained from GC with the average of four injections to calculate their Faradaic efficiencies. The gas product (H_2) from carbon dioxide electroreduction (CO_2RR) was analyzed using chromatograph (InterScience PerkinElmer Clarus 680) coupled with two thermal conductivity detector (TCD) and a flame ionization detector (FID), while the liquid product was analyzed using HPLC (Infinity 1260 II LC, Agilent Technologies. Hi-Plex H column (@ 50C) with VWD (@ 210 nm and 280 nm) and RID (@40 C). ^1H NMR was measured using Bruker 400 MHz and was processed in MestreNova and chemical shifts (δ) were reported in ppm.

Surface characterizations were performed using a Hitachi H7500 Scanning Electron Microscopy (SEM, Hitachi, Chiyoda, Tokyo, Japan) and a Quanta Feg 250 Field-Emission Scanning Electron Microscope. X-ray photoelectric spectroscopy (XPS) analyses were performed with a Theta-probe Thermo-Fisher Scientific Instrument (East Grinstead, UK) with a monochromatic Kα source with a photo energy of 1486.6 eV. The accumulated angle was 90° with a 20 eV pass energy at the analyser in an 8-10 mbar vacuum chamber. The spectra were processed using the system's software (Avantage v5.986). A modified Shirley background was used for the baseline. A 30% Lorentzian/Gaussian mix was used for symmetric peaks; however, this was allowed to vary for the asymmetric peaks (C 1s sp^2 peak, and the main Pd 3d spin-orbit pairs). The $3d_{3/2}$ features were constrained to the $3d_{5/2}$ features for both Sn_and Pd using the appropriate spin orbit parameters. This was also done for the Pd 3p spin-orbit pair as the O 1s peak overlaps with Pd $3p_{3/2}$ peak. Thus,

by collecting the Pd $3p_{1/2}$ and applying the spin-orbit parameters, the Pd $3p_{3/2}$ contribution to the O 1s peak intensity could be subtracted out.

Atomic Force Atomic force microscopy (AFM) was applied to characterize the surface microstructure of the deposited catalyst onto glassy carbon electrode. The Bruker's Dimension Icon equipped with TESPA-V2 tip performed the AFM characterization in a soft tapping mode. The height sensor and peak force error images of the catalyst layer were obtained during the test, and the 3D images were constructed based on the high sensor data by the NanoScope Analysis software.

X-ray diffraction (XRD) was performed using a Bruker D8 Advanced diffractometer with Cu-Kα source (Cu radiation wavelength: $K\alpha_1(100) = 1.54060$ Å, $K\alpha_2(50) = 1.54439$ Å) and Lynxeye-XE-T position sensitive detector. The aerogel was sprinkled on non-diffraction Si wafer substrate; however, the whole electrode is fixed on the sample stage with small displacement which is correct by Nickel metal peaks. The data were evaluated by Bruker software DiffracSuite.[1,2]

Part S3. Synthesis of the Sn-Pd Aerogels

The Sn-Pd hydrogels, were prepared using a simple procedure as demonstrated in our previous work.[1] First, an aqueous solution of sodium carbonate (Na_2CO_3) and glyoxylic acid with the ratio of 1:5, was added into a 10 mL solution of H_2PdCl_4 (0.2 mM) and $SnCl_2$ (0.1 mM) solution under stirring.[2] The mixture was sonicated for 10 minutes to achieve a bright yellow solution.[3] Next, the glassy vial containing the suspension was transferred into the oven and allowed to settle at 70 °C for 45 min to obtain a dark gray color. After cooling the solution to room temperature, 5 mg of $NaBH_4$ was added to complete reduction. Afterwards, the temperature was increased to 40 ℃ for another 3 h to form the Sn-Pd hydrogel.

After synthesizing the hydrogels, they were washed with distilled water, ethanol, and acetone (20 mL, 3 times each in sequences) followed by overnight freeze-drying using a lyophilizer to obtain porous Sn-Pd aerogels.[1] The Sn-Pd/CNT and the Sn-Pd/CNT-NH_2 aerogels were synthesised using a similar method by adding a 1:1 ratio of Sn-Pd and CNT/CNT-NH_2. To prepare the electrode, a portion of the ground aerogels was mixed with Nafion (2%), then 2 µL of the mixture was drop casted onto a glassy carbon electrode (GCE) with the surface area of 0.072 cm^2 and allowed to air dry.

Part S4. Electrochemical Measurements

The electrochemical studies were carried under CO_2/Ar in a sealed conditions using a CHI 660C potentiostat (CH Instruments, Austin, TX) with a three-electrode set up enclosed in Faraday cage including: 1) modified glassy carbon electrode with aerogel as working electrode; 2) Pt wire auxiliary electrode; 3) Ag/AgCl reference electrode. The glassy carbon surface was polished with 1, 0.3 and 0.05 μm alumina slurries, respectively, and ultrasonicated in acetonitrile, ethanol, and water. The electrodes were connected to the H-cell *via* a Nafion membrane. Linear sweep voltammetry (LSV) measurements were conducted with a positive initial scan polarity, 5 second quiet, and a scan rate of 0.1 V/s. All potentials were converted from Ag/AgCl (3 M KCl) to RHE ($E_{RHE}=E^0_{Ag/AgCl} + 0.0591 \times pH + 0.210$).

The reported Faradic efficiency (FE) and current density (*j*) are average values based on four reactions run with GC measurements taken every 15 min for 2 h.

The FE of the CO and H_2 products was *via* either Eq. S1:

Eq. S1:

$$FE = \frac{2 \times 96485\ (c/mol) \times V\ (mL/min) \times 10^{-6}\ (m^3/mL) \times v\ (vol.\%) \times 10^5\ (N/m^2)}{8.314\ (N.m/mol.K) \times 298.15K \times I_{total}\ (C/s) \times 60\ (s/min)}$$

v (vol.%) = Volume concentration of the products

V (mL/min) = Gas flow rate measured by a flow meter at room temperature under ambient pressure. I_{total} (C/s) = cell current.

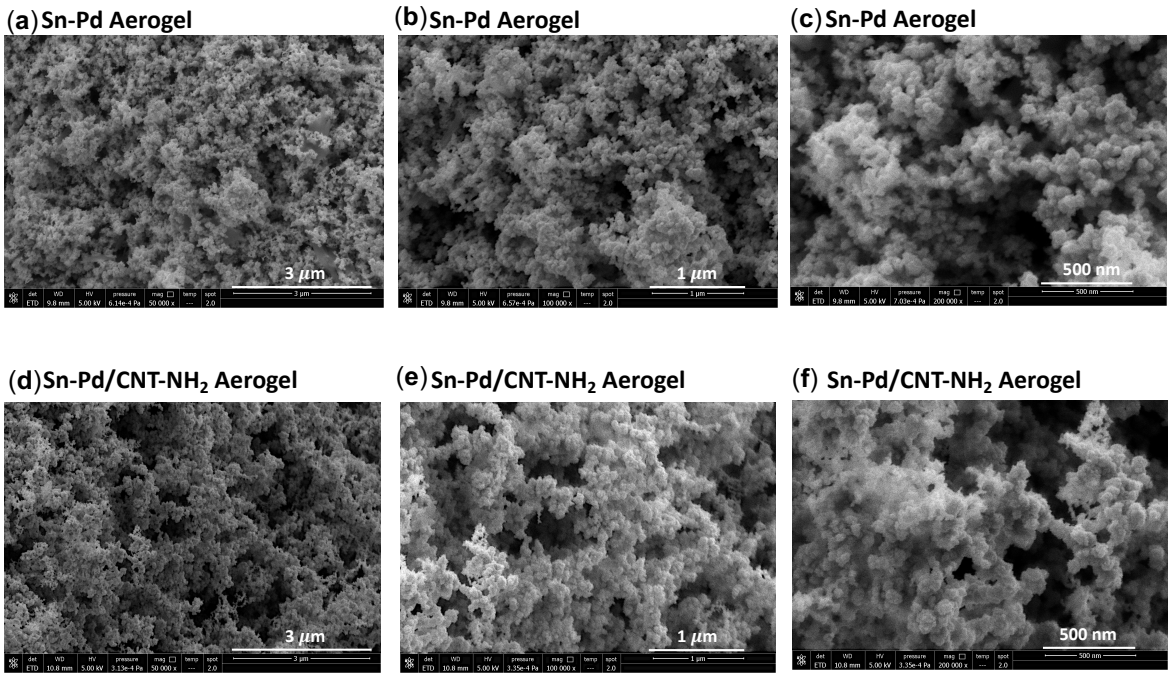

Figure S1. Scanning Electron Microscopy (SEM) of (a) Sn-Pd (scale bar: 3μm); (b) Sn-Pd (scale bar: 1μm); (c) Sn-Pd (scale bar: 500 nm); (d) Sn-Pd/CNT-NH_2 (scale bar: 3μm); (b) Sn-Pd/CNT-NH_2 (scale bar: 1μm); and (f) Sn-Pd/CNT-NH_2 (scale bar: 500 nm).

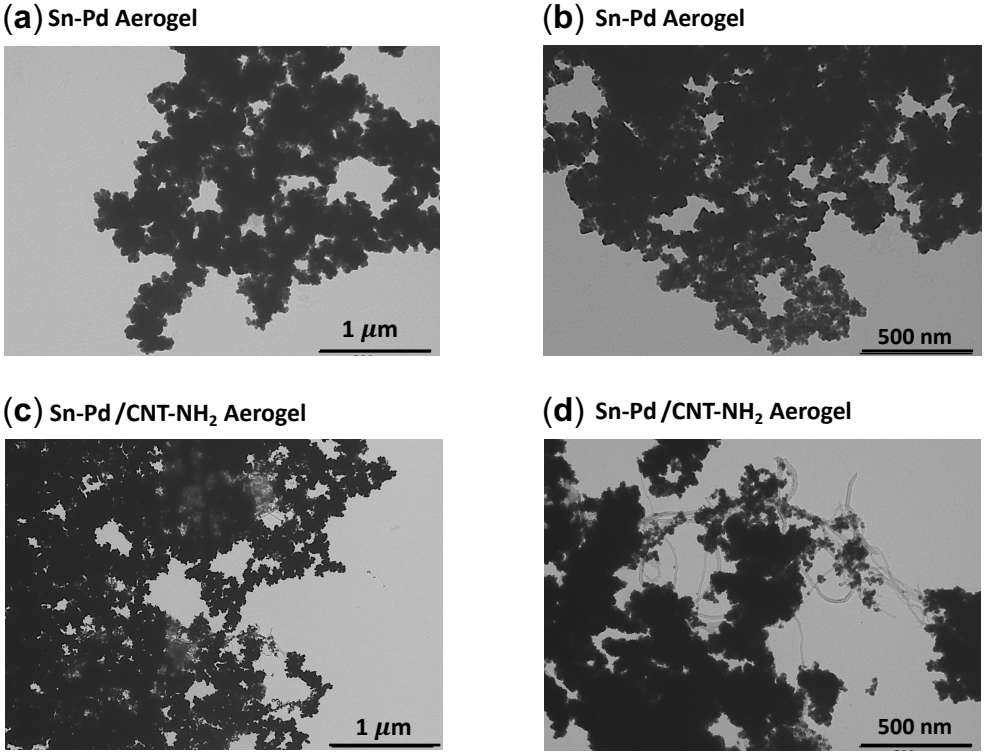

Figure S2. Transmission Electron Microscopy (TEM) of (a) Sn-Pd (scale bar: 1μm); (b) Sn-Pd (scale bar: 500 nm); (c) Sn-Pd/CNT-NH_2 (scale bar: 1μm); and (d) Sn-Pd/CNT-NH_2 (scale bar: 500 nm).

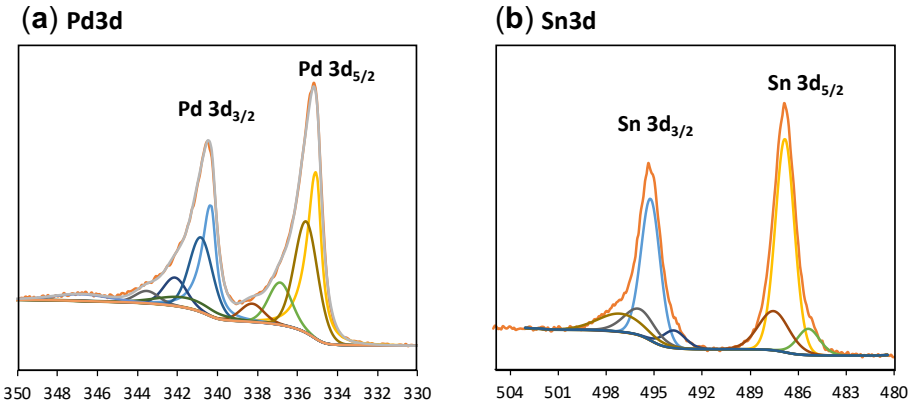

Figure S3. XPS spectra survey comparison of: (a) Pd3d; and (b) Sn3d spectra of the bimetallic Sn-Pd aerogel.

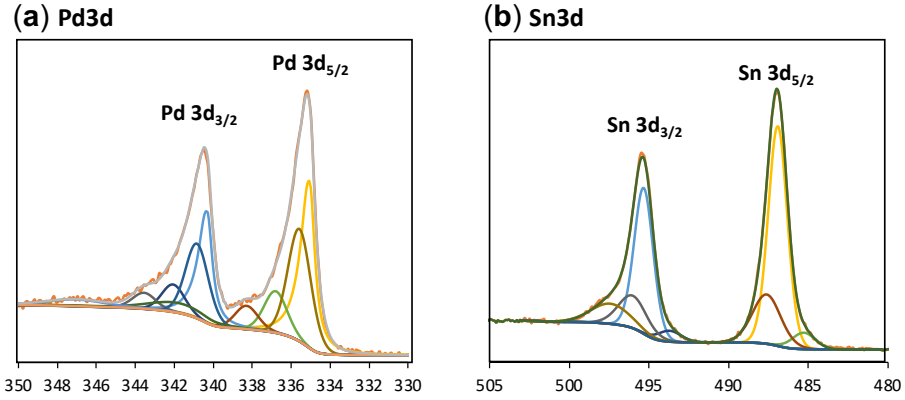

Figure S4. XPS spectra survey comparison of: (a) Pd3d; and (b) Sn3d spectra of the bimetallic Sn-Pd/CNT aerogel.

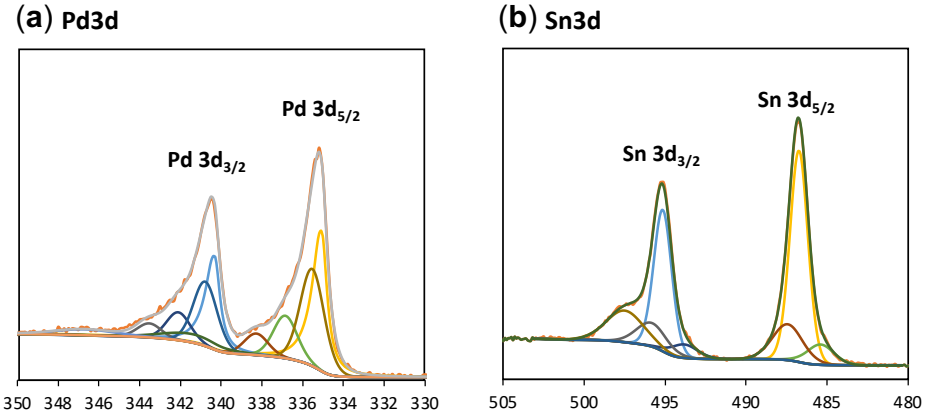

Figure S5. XPS spectra survey comparison of: (a) Pd3d; and (b) Sn3d spectra of the bimetallic Sn-Pd/CNT-NH_2 aerogel.

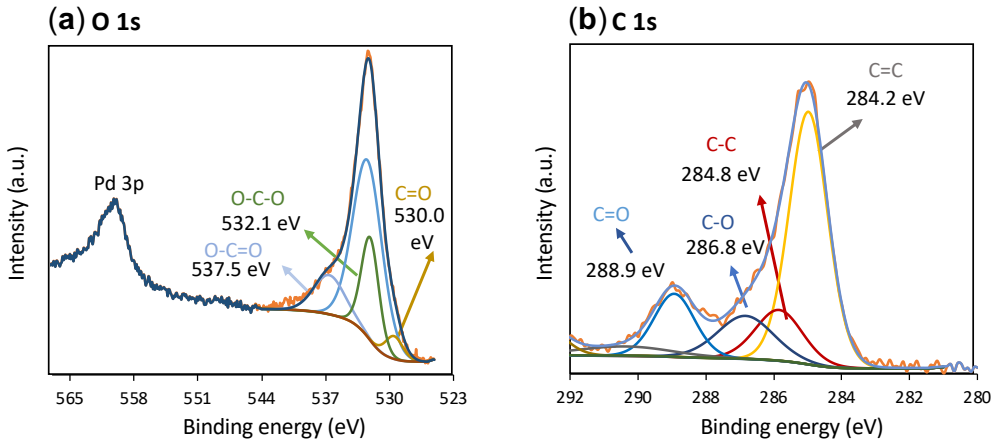

Figure S6. X-ray photoelectron spectroscopy (XPS) characterization of the monometallic Pd aerogel including (a) O 1s; and (b) C 1s spectra.

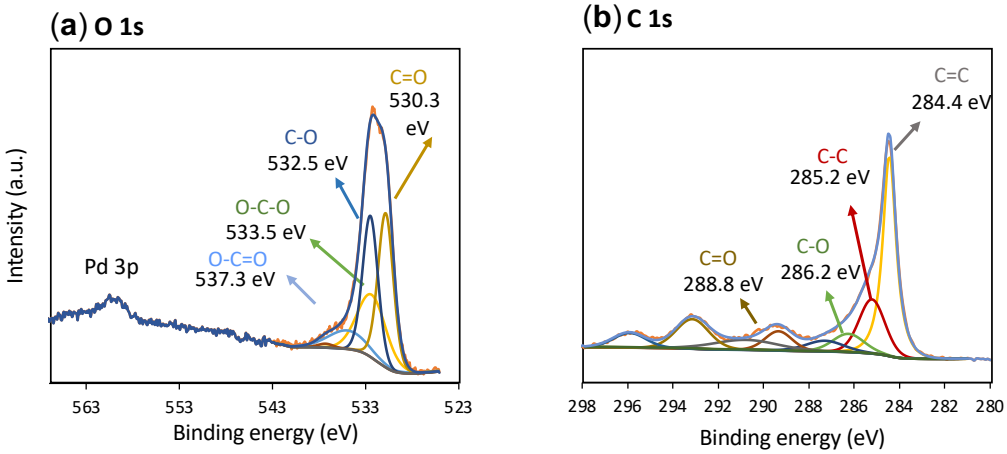

Figure S7. X-ray photoelectron spectroscopy (XPS) characterization of the bimetallic Sn-Pd aerogel including (a) O 1s; and (b) C 1s spectra.

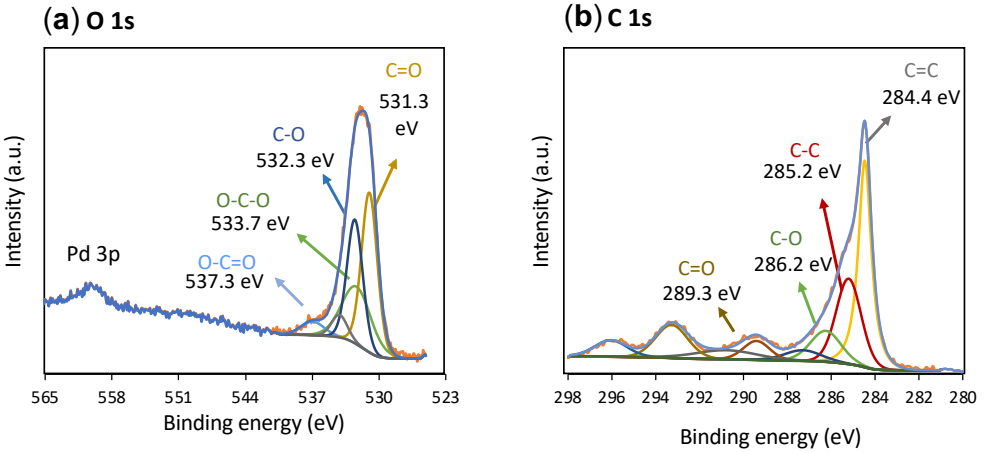

Figure S8. X-ray photoelectron spectroscopy (XPS) characterization of the bimetallic Sn-Pd/CNT aerogel including (a) O 1s; and (b) C 1s spectra.

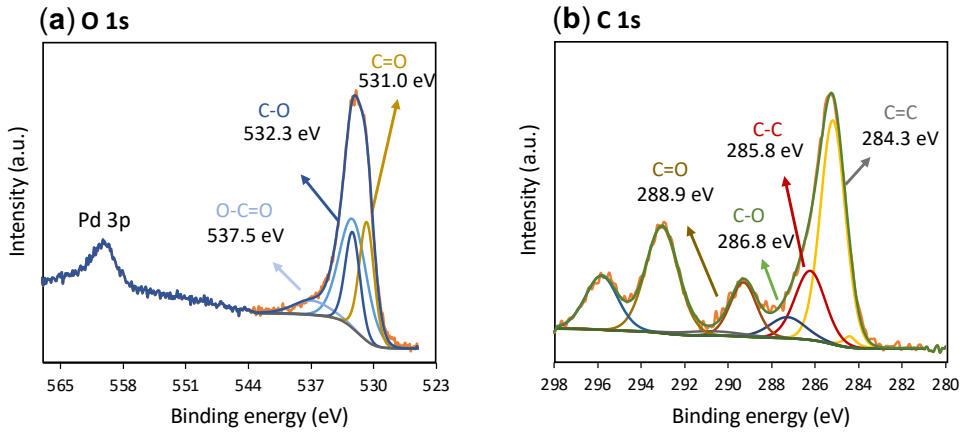

Figure S9. X-ray photoelectron spectroscopy (XPS) characterization of the bimetallic Sn-Pd/CNT-NH_2 aerogel including (a) O 1s; and (b) C 1s spectra.

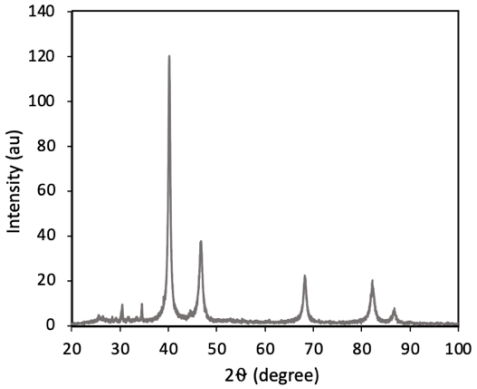

Figure S10. X-Ray Diffraction (XRD) patterns of Sn-Pd/CNT-NH_2

Part S5. Electrochemical active surface area measurement

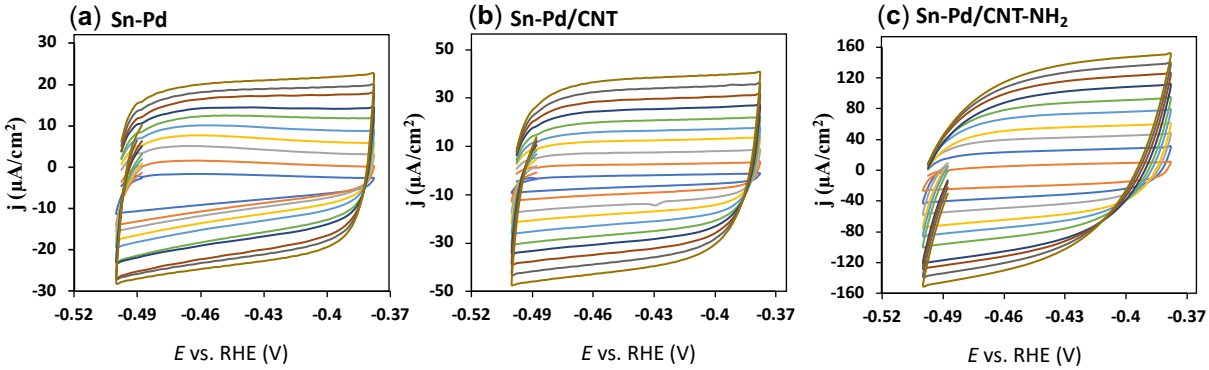

Figure S11. Double layer capacitances obtained from CV measurements. CV curves of a) Sn-Pd, b) Sn-Pd/MWCNT, and c) Sn-Pd/MWCNT-NH_2 between -0.50 and -0.38 V vs. Ag/AgCl and scan rates 10, 20, 30, 40, 50, 60, 70, 80, 90, and 100 mV/s.

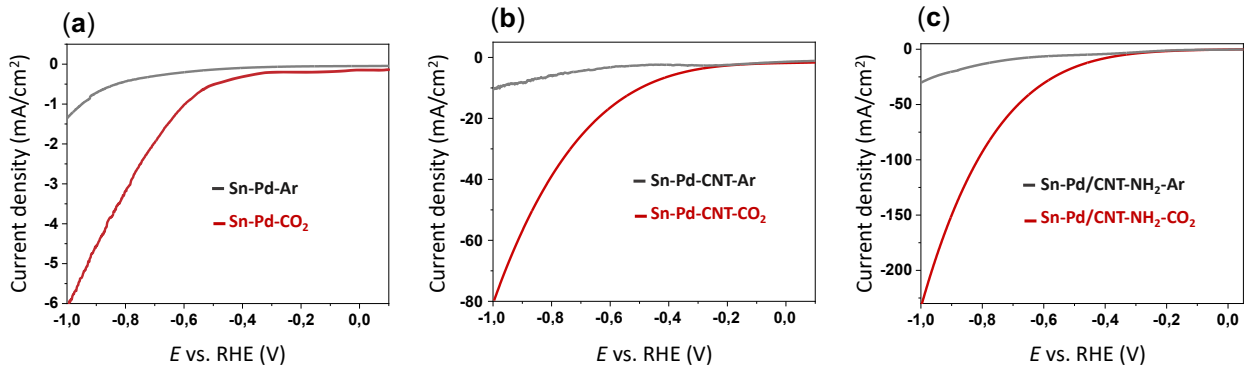

Figure S12. Linear sweep voltammetry (LSV) comparison of: (a) Sn-Pd, (b) Sn-Pd/CNT, and (c) Sn-Pd/CNT-NH_2 in 0.1 M $KHCO_3$.

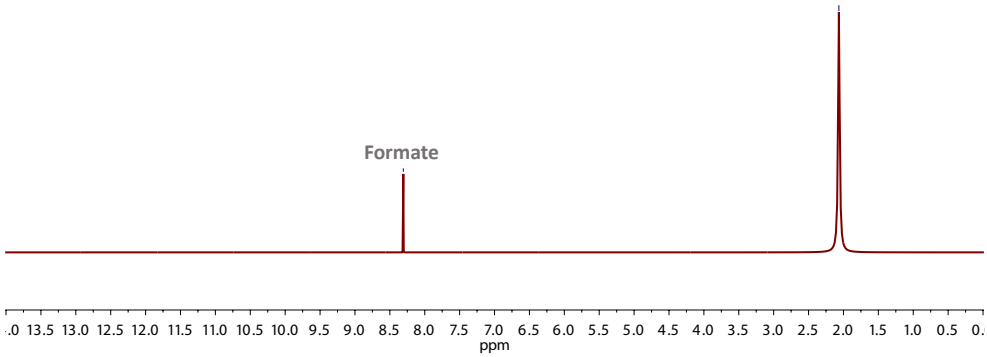

Figure S13. ^{1}H NMR spectra example of Sn-Pd/CNT-NH_2 after 2 h electrolysis

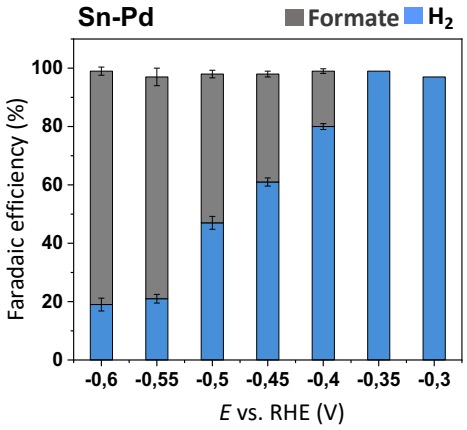

Figure S14. Faradic efficiency (FE) of Sn-Pd aerogel after 2 h electrolysis at -0.3, -0.35, -0.4, -0.45, -0.5, -0.55, and -0.6 V vs. RHE in 0.1 M $KHCO_3$.

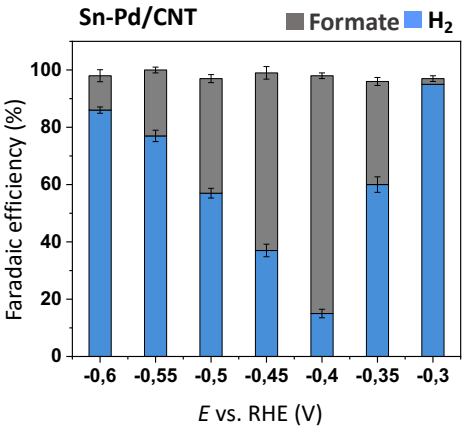

Figure S15. Faradic efficiency (FE) of Sn-Pd/CNT aerogel after 2 h electrolysis at -0.3, -0.35, -0.4, -0.45, -0.5, -0.55, and -0.6 V vs. RHE in 0.1 M $KHCO_3$.

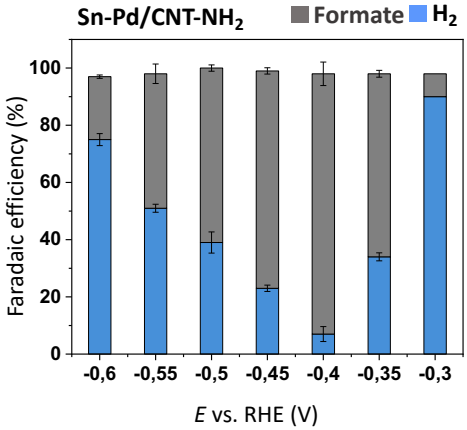

Figure S16. Faradic efficiency (FE) of Sn-Pd/CNT-NH_2 aerogel after 2 h electrolysis at -0.3, -0.35, -0.4, -0.45, -0.5, -0.55, and -0.6 V vs. RHE in 0.1 M $KHCO_3$.

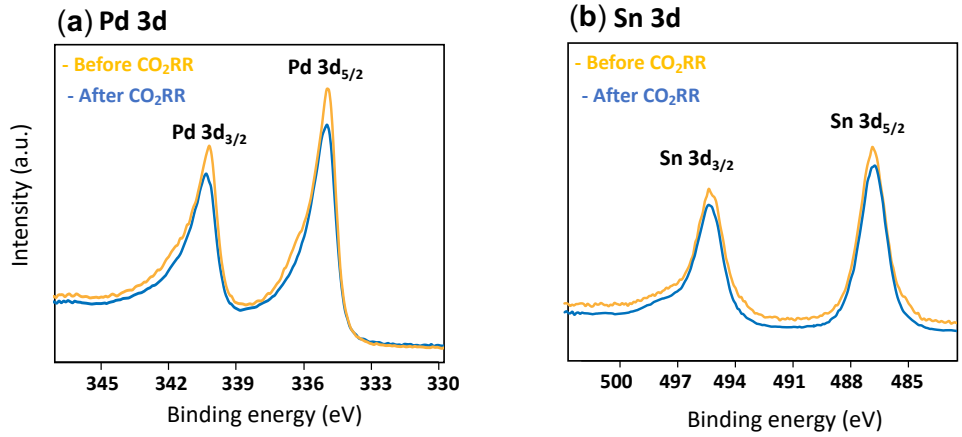

Figure S17. X-ray photoelectron spectroscopy (XPS) spectra survey comparison of: (a) Pd 3d, and Sn-Pd/CNT-NH_2 aerogels; (b) Sn 3d spectra of Sn-Pd/CNT-NH2 before and after electrochemical CO_2RR

In order to further monitor the stability and the chemical nature of -NH_2 in Sn-Pd/CNT-NH_2, FTIR measurements were performed before and after CO_2RR (Figure S19). The IR spectrum showed a characteristic peak at ~1600–1650 cm^{-1} belonging to the C═C of CNT. Similarly, the IR spectrum of CNT–NH_2 pictured a band at 1230 cm^{-1} corresponding to that of the C–N bond stretch. Characteristic peaks with wavenumbers of 2950–3000 cm^{-1} were assigned to C-H and N–H stretching bands.[20] This experiment showed no evidence of degradation of the functionalized CNT-NH_2, confirming the high stability of the aerogels. Furthermore, XPS comparison of Sn and Pd showed no noticeable shift after CO_2RR.

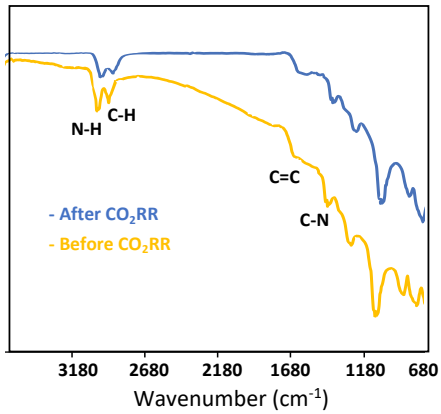

Figure S18. FTIR spectra of Sn-Pd/CNT-NH_2 before and after CO_2RR

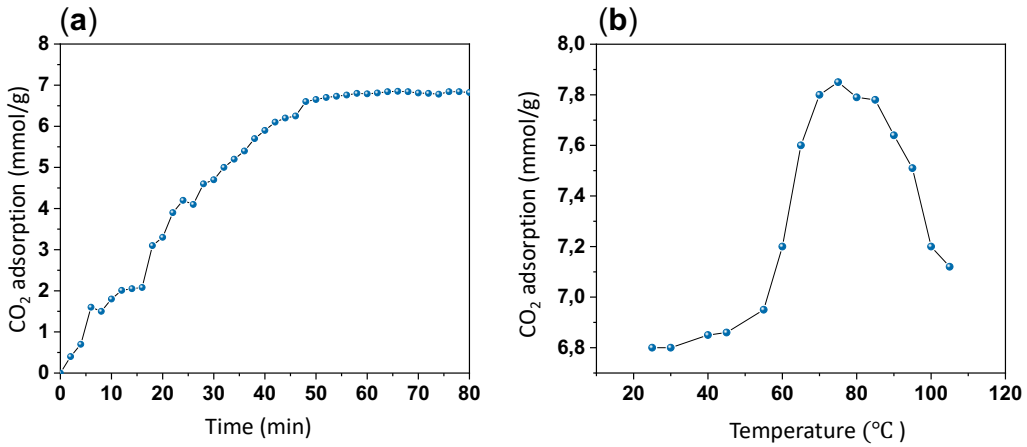

Figure S19. CO_2 adsorption of Sn-Pd/CNT-NH_2 at (a) room temperature over 80 minutes; and (b) variable temperature (25 ℃-110 ℃).

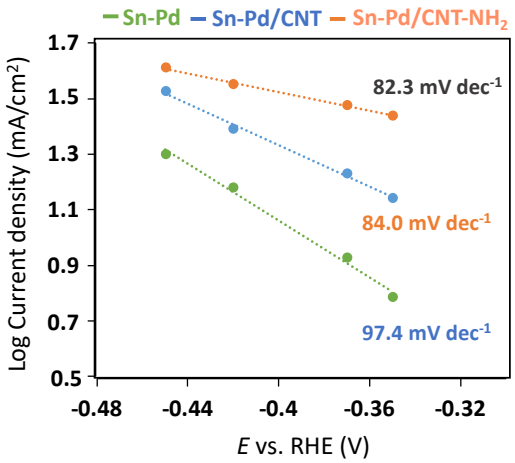

Figure S20. Tafel slopes for the current density of Sn-Pd, Sn-Pd/CNT, and Sn-Pd/CNT-NH_2 at -0.35, -0.37, -0.42 and, -0.45 V vs. RHE in 0.1 M $KHCO_3$.

Table S1. Product analysis of the synthesized aerogels after constant potential electrolysis. The reported data are the average values of three separate measurements from four separate reaction runs.

Catalyst	Electrolyte	V vs. RHE	*j* (mA/cm^2)	FE% (Formate)	FE% (H_2)	Ref.
Pd	$KHCO_3$ (0.1 M)	-0.3	-0.03	-	100	Current work
	$KHCO_3$ (0.1 M)	-0.35	-0.09	4±3.2	92±1.1	Current work
	$KHCO_3$ (0.1 M)	-0.4	-1.1	14±1.7	85±1.3	Current work
	$KHCO_3$ (0.1 M)	-0.45	-1.8	9±0.9	88±0.7	Current work
	$KHCO_3$ (0.1 M)	-0.5	-2.1	3±1.3	91±1.7	Current work
	$KHCO_3$ (0.1 M)	-0.55	-3.2	-	93±1.3	Current work
	$KHCO_3$ (0.1 M)	-0.6	-3.8	-	98±1.9	Current work

Catalyst	Electrolyte	V vs. RHE	*j* (mA/cm^2)	FE% (Formate)	FE% (H_2)	Ref.
Sn Nanoparticles	$KHCO_3$ (0.1 M)	-0.35	-0.08	-	100	Current work
	$KHCO_3$ (0.1 M)	-0.4	-0.10	-	100	Current work
	$KHCO_3$ (0.1 M)	-0.45	-0.11	-	100	Current work
	$KHCO_3$ (0.1 M)	-0.5	-0.12	-	94±1.1	Current work
	$KHCO_3$ (0.1 M)	-0.55	-0.14	11±1.2	82±1.9	Current work
	$KHCO_3$ (0.1 M)	-0.6	-0.18	17±1.8	83±1.1	Current work
Sn-Pd	$KHCO_3$ (0.1 M)	-0.3	-4.3	-	97	Current work
	$KHCO_3$ (0.1 M)	-0.35	-6.2	-	99	Current work
	$KHCO_3$ (0.1 M)	-0.4	-18.2	19±1	80±2.1	Current work
	$KHCO_3$ (0.1 M)	-0.45	-20.3	37±1	61±1.4	Current work
	$KHCO_3$ (0.1 M)	-0.5	-21.1	51±1.3	47±2.2	Current work
	$KHCO_3$ (0.1 M)	-0.55	-23.4	76±3.2	21±1.5	Current work
	$KHCO_3$ (0.1 M)	-0.6	-27.2	68±1.4	29±2.2	Current work
Sn-Pd/CNT	$KHCO_3$ (0.1 M)	-0.3	-11.3	2±1	95±0.7	Current work
	$KHCO_3$ (0.1 M)	-0.35	-14.1	36±1.4	60±2.7	Current work
	$KHCO_3$ (0.1 M)	-0.4	-29.6	83±1	15±1.5	Current work

Catalyst	Electrolyte	V vs. RHE	*j* (mA/cm^2)	FE% (Formate)	FE% (H_2)	Ref.
Sn-Pd/CNT	$KHCO_3$ (0.1 M)	-0.45	-34.2	62±2.2	37±2.2	Current work
	$KHCO_3$ (0.1 M)	-0.5	-37.1	40±1.4	56±1.7	Current work
	$KHCO_3$ (0.1 M)	-0.55	-39.3	23±1	77±2	Current work
	$KHCO_3$ (0.1 M)	-0.6	-44.0	12±2.1	86±1.1	Current work
Sn-Pd/CNT-NH_2	$KHCO_3$ (0.1 M)	-0.3	-19.6	8±1	90±1	Current work
	$KHCO_3$ (0.1 M)	-0.35	-27.3	64±1.2	34±1.4	Current work
Sn-Pd/CNT-NH_2	$KHCO_3$ (0.1 M)	-0.4	-39.1	91±1.4	7±2.6	Current work
	$KHCO_3$ (0.1 M)	-0.45	-40.7	76±1.1	23±1.1	Current work
	$KHCO_3$ (0.1 M)	-0.5	-43.2	61±1.1	39±3.7	Current work
	$KHCO_3$ (0.1 M)	-0.55	-44.6	47±3.4	51±1.4	Current work
	$KHCO_3$ (0.1 M)	-0.6	-51.2	22±0.6	75±2.1	Current work

Table S2. Previous report results comparison

Catalyst	Electrolyte	V vs. RHE	*j* (mA/cm^2)	FE% (Formate)	Ref.
Sn dendrite electrode	$KHCO_3$ (0.1 M)	-1.36	-17	71.6	[4]
Sn nanoparticles/Au	$KHCO_3$ (0.1 M)	-0.75	-42	30.2	[5]
Sn/SnO_x thin film	$KHCO_3$ (0.5 M)	-0.7	0.7	40	[6]
Wire-in-tube SnO_2	$KHCO_3$ (0.1 M)	-0.99	-3.8	63	[7]
SnO_2 porous NWs	$KHCO_3$ (0.1 M)	-0.8	-4.8	80	[8]
Sn gas diffusion electrode	$KHCO_3$ (0.1 M	-1.2	-3	64	[9]
Nanoporous In-Sn	$KHCO_3$ (0.1 M	-0.6	-9.6	78.6	[10]
$Ag_{76}Sn_{24}$	$KHCO_3$ (0.5 M	-0.8	-19.7	80	[11]
Sn rod	pure water	-0.98	-	94	[12]
Sn-CF1000	$KHCO_3$ (0.1 M)	-0.89	-11	62	[13]
Cu-Sn_3	$KHCO_3$ (0.1 M)	-0.5	-33	95	[14]
$Cu_{0.2}$-$Sn_{0.8}$	$KHCO_3$ (0.5 M)	-0.35	-	85	[15]
$Sn_{56.3}Pb_{43.7}$	$KHCO_3$ (0.5 M)	-1.37	45.7	79.3	[16]
Sn (S)-Au	$KHCO_3$ (0.1 M)	-0.75	55	93.3	[5]
Ni-SnS2	$KHCO_3$ (0.1 M)	-0.9	19.6	93	[17]

SnO_2 QWs/GBs	**$KHCO_3$ (0.1 M)**	**-1.5**	**13.7**	**80**	[18]
Mn-doped SnO_2		-1.05	21.2	85	[19]

Part S5. References

1 M. Abdinejad, C. Ferrag, M. N. Hossain, M. Noroozifar, K. Kerman and H. B. Kraatz, *J. Mater. Chem. A*, 2021, **9**, 12870–12877.

2 A. Shafaei Douk, H. Saravani and M. Noroozifar, *Electrochim. Acta*, 2018, **275**, 182–191.

3 A. S. Douk, H. Saravani, M. Z. Yazdan Abad and M. Noroozifar, *Compos. Part B Eng.*, 2019, **172**, 309–315.

4 D. H. Won, C. H. Choi, J. Chung, M. W. Chung, E.-H. Kim and S. I. Woo, *ChemSusChem*, 2015, **8**, 3092–3098.

5 X. Zheng, P. De Luna, F. P. García de Arquer, B. Zhang, N. Becknell, M. B. Ross, Y. Li, M. N. Banis, Y. Li, M. Liu, O. Voznyy, C. T. Dinh, T. Zhuang, P. Stadler, Y. Cui, X. Du, P. Yang and E. H. Sargent, *Joule*, 2017, **1**, 794–805.

6 Y. Chen and M. W. Kanan, *J. Am. Chem. Soc.*, 2012, **134**, 1986–1989.

7 L. Fan, Z. Xia, M. Xu, Y. Lu and Z. Li, *Adv. Funct. Mater.*, 2018, **28**, 1706289.

8 B. Kumar, V. Atla, J. P. Brian, S. Kumari, T. Q. Nguyen, M. Sunkara and J. M. Spurgeon, *Angew. Chemie Int. Ed.*, 2017, **56**, 3645–3649.

9 J. Wu, F. G. Risalvato, S. Ma and X.-D. Zhou, *J. Mater. Chem. A*, 2014, **2**, 1647–1651.

10 W. J. Dong, C. J. Yoo and J.-L. Lee, *ACS Appl. Mater. Interfaces*, 2017, **9**, 43575–43582.

11 W. Luc, C. Collins, S. Wang, H. Xin, K. He, Y. Kang and F. Jiao, *J. Am. Chem. Soc.*, 2017, **139**, 1885–1893.

12 V. S. K. Yadav, Y. Noh, H. Han and W. B. Kim, *Catal. Today*, 2018, **303**, 276–281.

13 Y. Zhao, J. Liang, C. Wang, J. Ma and G. G. Wallace, *Adv. Energy Mater.*, 2018, **8**, 1702524.

14 X. Zheng, Y. Ji, J. Tang, J. Wang, B. Liu, H.-G. Steinrück, K. Lim, Y. Li, M. F. Toney, K. Chan and Y. Cui, *Nat. Catal.*, 2019, **2**, 55–61.

15 J. He, K. E. Dettelbach, A. Huang and C. P. Berlinguette, *Angew. Chemie Int. Ed.*, 2017, **56**, 16579–16582.

16 S. Y. Choi, S. K. Jeong, H. J. Kim, I.-H. Baek and K. T. Park, *ACS Sustain. Chem. Eng.*, 2016, **4**, 1311–1318.

17 A. Zhang, R. He, H. Li, Y. Chen, T. Kong, K. Li, H. Ju, J. Zhu, W. Zhu and J. Zeng, *Angew.*

Chemie Int. Ed., 2018, **57**, 10954–10958.

18 S. Liu, J. Xiao, X. F. Lu, J. Wang, X. Wang and X. W. (David) Lou, *Angew. Chemie Int. Ed.*, 2019, **58**, 8499–8503.

19 Y. Wei, J. Liu, F. Cheng and J. Chen, *J. Mater. Chem. A*, 2019, **7**, 19651–19656.